Synthesis of buckhorn-like BiVO$_4$ with a shell of CeO$_x$ nanodots: Effect of heterojunction structure on the enhancement of photocatalytic activity

Shaonan Gu, Wenjun Li*, Fangzhi Wang, Shuyun Wang, Hualei Zhou, Hongda Li

Beijing Key Laboratory for Science and Application of Functional Molecular and Crystalline Materials, University of Science and Technology Beijing, Beijing 100083, China

ABSTRACT

Composite photocatalysts CeO$_x$/BiVO$_4$ with a heterojunction structure were synthesized using hydrothermal and ion-impregnation method. The composites were characterized by X-ray diffraction, BET, high-resolution transmission electron microscopy, selected area electron diffraction, and X-ray photoelectron spectroscopy. UV–vis diffuse reflectance spectroscopy was used to investigate the absorption range and band gap of photocatalysts. The photocatalytic activities of the prepared samples were also examined by studying the degradation of methylene blue under visible-light irradiation. Results showed that the composite with 5.7 wt.% CeO$_x$/BiVO$_4$ exhibited the highest photocatalytic activity within the studied range. The separation of the photogenerated charge and the effect of heterojunction structure on photocatalytic activities could be well interpreted based on the heterojunction structure with consideration of the Fermi level. The charge-separation process and the important role of deposited cerium were proven by photoluminescence spectroscopy and electron paramagnetic resonance spectra. Results demonstrated that the heterojunction structure and the electron-trapping effect of cerium greatly depressed the recombination of photogenerated charges in the composites.

© 2015 Elsevier B.V. All rights reserved.

1. Introduction

Bismuth vanadate (BiVO$_4$) has recently become a very attractive material as a promising photocatalyst for organic pollutant decomposition working under visible-light [1,2]. With a narrow band gap of about 2.4 eV, BiVO$_4$ possesses an excellent ability of absorbing visible-light abundant in the solar spectrum. However, the photocatalytic activity of BiVO$_4$ is usually not satisfied because photogenerated electron–hole pairs tend to decay rapidly through recombination. The low charge-separation efficiency may be the main obstacle restricting the practical applications of BiVO$_4$. Therefore, tremendous efforts have been made to develop effective strategies to improve the visible-light photocatalytic activity of BiVO$_4$ photocatalysts.

Composite materials with a heterojunction structure have been widely investigated in photocatalysis and solar energy conversion [3,4] because the heterojunction structure dominates the direction of transport and the recombination rate of the photogenerated charge in composite materials. Heterojunction is generally constructed in composite materials between semiconductors with matching band potentials. This procedure results in the construction of a contact electric field at this heterojunction interface [5]. During irradiation, the photogenerated charges can transport from one semiconductor to another and are driven by the internal electric field to improve separation [6,7]. Accordingly, coupling BiVO$_4$ with another semiconductor with matching band potentials to design heterojunction structure is an active strategy of improving the charge-separation efficiency and obtaining a satisfied photocatalytic activity under visible-light. Several studies have focused on the BiVO$_4$-based composite photocatalysts, such as Co$_3$O$_4$/BiVO$_4$ [8], CuO/BiVO$_4$ [8–10], WO$_3$/BiVO$_4$ [11], FeO/BiVO$_4$ [12], V$_2$O$_5$/BiVO$_4$ [13,14], BiVO$_4$/TiO$_2$ [15,16], and even V$_2$O$_5$/TiO$_2$/BiVO$_4$ [17]. These composites have been demonstrated to be effective in enhancing the photocatalytic activity of BiVO$_4$. However, the detailed mechanism of the electron–hole pair separation and the nature of the composite material in improving the photocatalytic activity of BiVO$_4$ have not yet been entirely understood.

* Corresponding author at: University of Science & Technology Beijing, Department of Chemistry, No. 30 Xueyuan Rd., Haidian District, Beijing 100083, China. Tel.: +86 10 62332468.
E-mail address: wjli_ustb@163.com (W. Li).

This study reports a novel $CeO_x/BiVO_4$ composite photocatalyst to further investigate the effect of the heterojunction structure and the deposited component on enhancing the photocatalytic activity of $BiVO_4$ under visible-light. Lanthanide ions or oxides are used to modify TiO_2 to obtain a high performance in photodecomposition [18,19]. However, these chemicals have little application in modifying $BiVO_4$ to improve the photocatalytic activity. This study synthesizes $BiVO_4$ coupled with different cerium contents. Furthermore, the plausible mechanism of the photogenerated charge separation and the effect of the heterojunction structure are interpreted. The electron-trapping effect of cerium in the heterojunction structure is proposed and indirectly proved.

2. Experimental

2.1. Synthesis of $CeO_x/BiVO_4$ composite photocatalysts

All chemicals used in this work were of analytical reagent grade (Sinopharm Chemical Reagent Co., Ltd., China) and used without further purification. The solutions were prepared using Milli-Q water. The $CeO_x/BiVO_4$ composite photocatalysts were prepared using hydrothermal and ion-impregnation method. Subsequently, 4 mmol $Bi(NO_3)_3 \cdot 5H_2O$ was dissolved in nitric acid and Milli-Q water to form a 100 mL transparent solution. Afterwards, 4 mmol NH_4VO_3 was dissolved in 100 mL Milli-Q water at 70 °C. These two solutions were then mixed together, and the mixture was stirred for about 30 min to obtain a stable yellow slurry at room temperature. The pH value was adjusted to ca. 4 with ammonia. The yellow slurry was transferred into Teflon-lined stainless steel autoclaves. The sealed reactors were then heated at 180 °C for 6 h. The precipitate was subsequently filtered and washed with Milli-Q water several times to ensure that the residual impurities were removed. The precipitate was then dried at 80 °C for 6 h. Six copies of 600 mg $BiVO_4$-obtained samples were immersed into 20 mL Ce^{3+} solutions with different amounts of $Ce(NO_3)_3 \cdot 6H_2O$ (i.e., 18.7, 37.2, 74.4, 112, 149, and 187 mg) added in, respectively. The suspensions were stirred using a glass rod during water evaporation on a heating jacket. The dried powders were calcined at 400 °C for 4 h. The $CeO_x/BiVO_4$ composite photocatalysts were then obtained. Meanwhile, 600 mg $Ce(NO_3)_3 \cdot 6H_2O$ was dissolved in 20 mL Milli-Q water followed by water evaporation and calcination. Pure CeO_x powder was obtained under the same conditions.

2.2. Characterization

The crystalline phases of pure $BiVO_4$ and $CeO_x/BiVO_4$ were determined using X-ray diffraction (XRD) (D/MAX-RB, Rigaku, Japan). The diffraction patterns were recorded in the $2\theta = 10–70°$ range with a Cu Kα source ($\lambda = 0.15405$) running at 40 kV and 30 mA. The specific surface area of pure $BiVO_4$ and composites was determined by Brunauer–Emmett–Teller (BET) method (NOVA 4200e, Quantchrome, USA). The samples were outgassed at 300 °C under vacuum for 4 h prior to measurement. Their N_2 adsorption and desorption isotherms at 77 K under different partial pressures were then measured. The high-resolution transmission electron microscopy (HRTEM) images and the selected area electron diffraction (SAED) patterns were recorded on a transmission electron microscope (F-20, FEI, USA) at an accelerating voltage of 200 kV. X-ray photoelectron spectroscopy (XPS) was performed on an X-ray photoelectron spectrometer (AXIS ULTRA^{DLD}, Kratos, Japan) using the Al Kα radiation. The UV–vis diffuse reflectance (DRS) spectra of the photocatalysts were recorded at room temperature in the 300–800 nm range using a UV–vis spectrophotometer (U-3900H, Hitachi, Japan) equipped with an integrating sphere. $BaSO_4$ was used as the reference. The photoluminescence (PL)

spectra were recorded using a fluorescence spectrophotometer (F-4500, Hitachi, Japan) with a Xe lamp as the excitation light source. In order to detect the generation of activated species, the electron paramagnetic resonance (EPR) spectra were performed on an EPR spectrometer (EMX Plus, Bruker, Germany). The spectra were obtained using the microwave power of 20 mW, frequency of 9.85 GHz and 3503 G central magnetic field.

2.3. Measurement of photocatalytic activity

The photocatalytic activities of the $BiVO_4$, CeO_x and $CeO_x/BiVO_4$ composite photocatalysts under visible-light were evaluated by degrading methylene blue (MB) with an initial dye concentration of 3×10^{-5} mol/L. A 100 W incandescent lamp with an UV-cutoff filter ($\lambda > 420$ nm) was used as a light source and set about 10 cm apart from the reactor. The experiments were performed at ambient temperature as follows: 50 mg photocatalyst was dispersed in 50 mL of MB solution followed by stirring for 60 min in the dark to achieve an adsorption–desorption equilibrium before light irradiation. During the irradiation, the reaction samples were collected at 30 min intervals and centrifuged to remove the photocatalyst particles. The ratio (C/C_0) of the MB concentration was adopted to evaluate the degradation efficiency (i.e., C_0 was the MB concentration at the time of the adsorption–desorption equilibrium, where C was the MB concentration at certain time) by checking the absorbance spectrum at 664 nm using a UV–vis spectrophotometer (U-3900H, Hitachi, Japan).

3. Results and discussion

3.1. XRD analysis

Three crystalline phases were reported for the synthesized $BiVO_4$: monoclinic scheelite-type, tetragonal scheelite-type, and tetragonal zircon-type. However, only the monoclinic scheelite structure $BiVO_4$ showed good photocatalytic performance under visible-light irradiation [20,21]. Fig. 1(A) presents the XRD diffraction patterns of the pure $BiVO_4$ and $CeO_x/BiVO_4$ series of composite photocatalysts. All the photocatalysts had a single monoclinic $BiVO_4$ structure. The typical diffraction peaks of 18.5°, 19.1°, 28.8°, 30.5°, 34.6°, 35.3°, 39.8°, and 42.4° of all the patterns at 2θ were respectively indexed as (1 1 0), (0 1 1), (1 2 1), (0 4 0), (2 0 0), (0 0 2), (1 4 1), and (1 5 0) planes of the monoclinic $BiVO_4$ based on the JCPDS card no. 14-0688. No signals for any crystalline phases of cerium were detected in the composite photocatalysts because of their low Ce content. Fig. 1(B) shows the shift of the peaks at about 2θ of 28.8° and 30.5°, which corresponded to the (1 2 1) and (0 4 0) planes, respectively. Different levels of shifts were found in these peaks depending on the deposition of the cerium component on the $BiVO_4$ surface, which suggested that the Ce composition in heterojunction led to a tiny change in their local crystal structures.

Table 1 presents the results of the surface area, lattice parameters and crystal size of the $BiVO_4$ and $CeO_x/BiVO_4$ composite photocatalysts. Little change is clearly seen in the lattice parameters and crystal size of the $BiVO_4$ and $CeO_x/BiVO_4$ series. The composite photocatalysts kept the same monoclinic scheelite structure as for pure $BiVO_4$, which indicated that cerium metal oxides may be merely loaded on the $BiVO_4$ surface to form a heterojunction without being anchored into the crystal lattice.

3.2. Morphology characterization

Fig. 2 illustrates the TEM images of the pure $BiVO_4$ and $CeO_x/BiVO_4$ composite photocatalysts. The morphology of the pure $BiVO_4$ (Fig. 2A) shows buckhorn-like nanoparticles, which are no
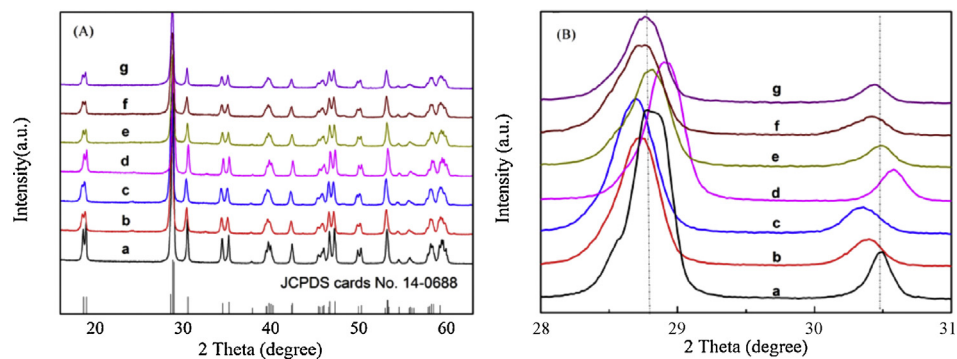
Fig. 1. (A) XRD patterns and (B) XRD peaks in (1 2 1) and (0 4 0) lattice planes of different photocatalysts: (a) pure BiVO$_4$, (b) 1 wt.% CeO$_x$/BiVO$_4$, (c) 1.96 wt.% CeO$_x$/BiVO$_4$, (d) 3.8 wt.% CeO$_x$/BiVO$_4$, (e) 5.7 wt.% CeO$_x$/BiVO$_4$, (f) 7.4 wt.% CeO$_x$/BiVO$_4$, and (g) 9 wt.% CeO$_x$/BiVO$_4$.

Table 1
Surface area, crystal sizes and lattice parameter of the pure BiVO$_4$ and CeO$_x$/BiVO$_4$ series of composite photocatalysts.

Photocatalyst	Surface area (m^2/g)	Crystal vol. (Å^3)	Lattice parameters		
			a (Å)	b (Å)	c (Å)
Pure BiVO$_4$	33.11	310.75	5.202	11.712	5.100
1 wt.% CeO$_x$/BiVO$_4$	51.27	312.10	5.208	11.729	5.109
1.96 wt.% CeO$_x$/BiVO$_4$	50.44	312.81	5.211	11.735	5.116
3.8 wt.% CeO$_x$/BiVO$_4$	50.42	308.95	5.187	11.701	5.091
5.7 wt.% CeO$_x$/BiVO$_4$	42.75	310.89	5.198	11.707	5.109
7.4 wt.% CeO$_x$/BiVO$_4$	17.84	310.96	5.197	11.722	5.105
9 wt.% CeO$_x$/BiVO$_4$	9.69	310.81	5.209	11.688	5.105
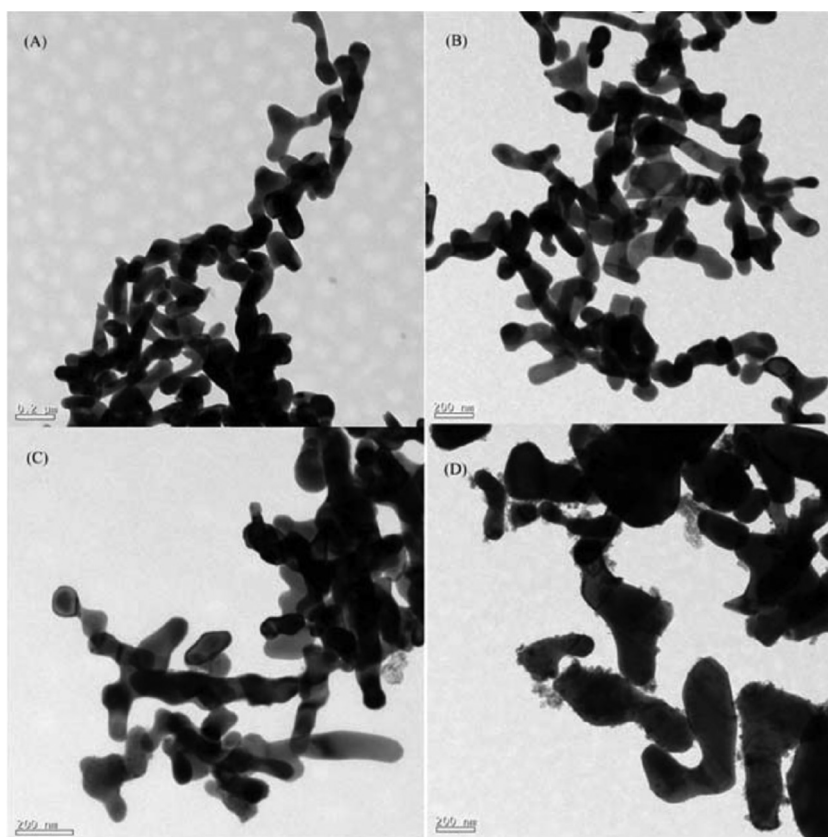
Fig. 2. TEM images of (A) pure BiVO$_4$, (B) 1.96 wt.% CeO$_x$/BiVO$_4$, (C) 5.7 wt.% CeO$_x$/BiVO$_4$ and (D) 9 wt.% CeO$_x$/BiVO$_4$ composite photocatalysts.

more than 100 nm wide and with each brand measuring hundreds of nanometers long. And the surface area of the pure BiVO$_4$ is 33.11 m^2/g according to Table 1. The composite photocatalysts in Fig. 2(B)–(D) clearly kept the same buckhorn-like morphology

as that of pure BiVO$_4$. However, the nanoparticle size obviously increased after cerium was introduced. The size of the buckhorn-like particles was close to the micro region, especially when the cerium content was up to 9 wt.%. This result implied that the
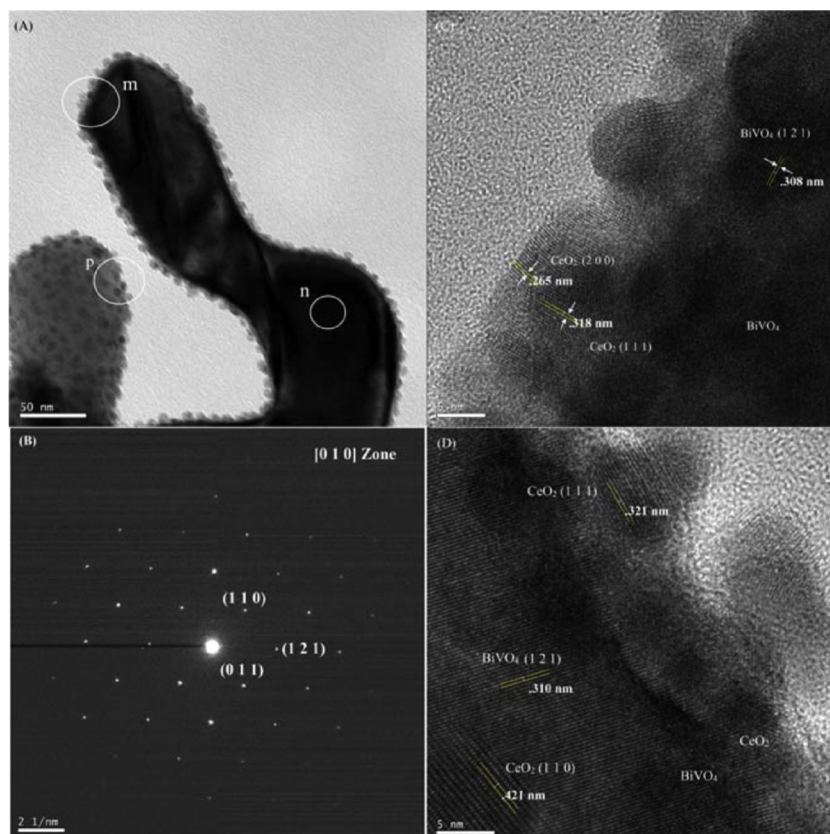
Fig. 3. TEM image (A) of an individual 5.7 wt.% CeO$_x$/BiVO$_4$ nanoparticles and HRTEM images (C, D) of the BiVO$_4$ substrate and CeO$_x$ nanodots marked as m and p in (A) respectively; (B) SAED pattern of a branch marked as n in (A).

deposition of the low cerium oxide content might thicken the substrate width. Meanwhile, the surface area in Table 1 also confirmed that when the cerium content was 7.4 wt.% and 9 wt.%, the surface area of the samples decreased to 17.84 m^2/g and 9.96 m^2/g respectively, corresponding to the size of micro region. The surface-deposited cerium oxides probably combined the adjacent BiVO$_4$ nanoparticles into a bigger one when the cerium concentration was higher than 5.7 wt.% after the calcination process (Fig. 2(D)). The TEM images also showed this finding to be true for the composite photocatalysts of 1 wt.% CeO$_x$/BiVO$_4$, 3.8 wt.% CeO$_x$/BiVO$_4$, and 7.4 wt.% CeO$_x$/BiVO$_4$, which were not displayed here.

The high-resolution transmission electron microscopy is an efficient and widely used characterization in terms of heterojunction [13,15], which was used to prove heterojunction formation in the CeO$_x$/BiVO$_4$ composite photocatalyst in this study. Fig. 3 shows the TEM image and HRTEM images of an individual 5.7 wt.% CeO$_x$/BiVO$_4$ composite photocatalysts. The high-magnification TEM image clearly confirmed that cerium oxide nanodots with ca. 5 nm diameter uniformly attached onto the surface of the BiVO$_4$ nanoparticles (Fig. 3(A)). The surface area of the samples demonstrated that the loaded cerium oxide nanodots made the surface area of BiVO$_4$ increase from about 30 m^2/g up to 50 m^2/g when the cerium content was no more than 5.7 wt.% (Table 1). The spacing of 0.473, 0.310, and 0.468 nm calculated from the selective area electron diffraction spots in Fig. 3(B) agreed well with the interplanar spacing of (1 1 0), (1 2 1) and (0 1 1) lattice planes of the monoclinic BiVO$_4$. These results indicated the single-crystal nature of the BiVO$_4$ nanoparticles. Fig. 3(C) and (D) presents the HRTEM images recorded from the branches in Fig. 3(A) marked as m and p, respectively. The two crystal structures with different interplanar spacing composites are clearly presented together in the HRTEM images. The interplanar spacing of 0.308 and 0.310 nm

corresponded to the (1 2 1) lattice planes of the monoclinic BiVO$_4$ based on the JCPDS card no. 14-0688. The interplanar spacing of 0.265, 0.421, and 0.318 nm for the cerium oxide nanodots agreed with the face-centered cubic structure CeO$_2$, which corresponded to the (2 0 0), (1 1 1), and (1 1 1) lattice planes, respectively [22]. This result revealed that the cerium oxide nanodots tightly contacted with the substrate of the BiVO$_4$ nanoparticles, which resulted in the formation of the heterojunction nanostructure on the surface of the BiVO$_4$ nanoparticles (Fig. 3(C) and (D)).

3.3. Chemical state analysis

The XPS analysis was used to further understand the chemical state of the CeO$_x$/BiVO$_4$ composite photocatalysts, especially the chemical state of cerium in the heterojunction nanostructure, which significantly influences the photocatalytic performance. Fig. 4(A) shows the overall XPS spectra of the CeO$_x$/BiVO$_4$ composite photocatalyst. The characteristic peaks of the Bi, Ce, V, and O elements were detected. Moreover, the observed peak of C 1s at 283.18 eV was attributed to the signal from carbon in the instrument [23]. Before the analysis, all peaks of the other elements were calibrated according to the deviation between the C 1s peak and the standard signal of C 1s at 284.8 eV. No XPS characteristic peaks of N 1s was detected at around 400 eV although the raw material ammonium metavanadate contained nitrogen element, which indicated no nitrogen doped in the CeO$_x$/BiVO$_4$ composite photocatalyst. The XPS signals located at 159.44 and 164.68 eV were attributable to Bi 4$f_{7/2}$ and Bi 4$f_{5/2}$, respectively (Fig. 4(B)). This finding confirmed that the bismuth species in the CeO$_x$/BiVO$_4$ composite photocatalyst was a Bi^{3+} cation. The peaks for O 1s located at 530.02 eV corresponded to the O^{2-} anion (Fig. 4(C)). No difference in the XPS peak position of O 1s was observed because of their similar
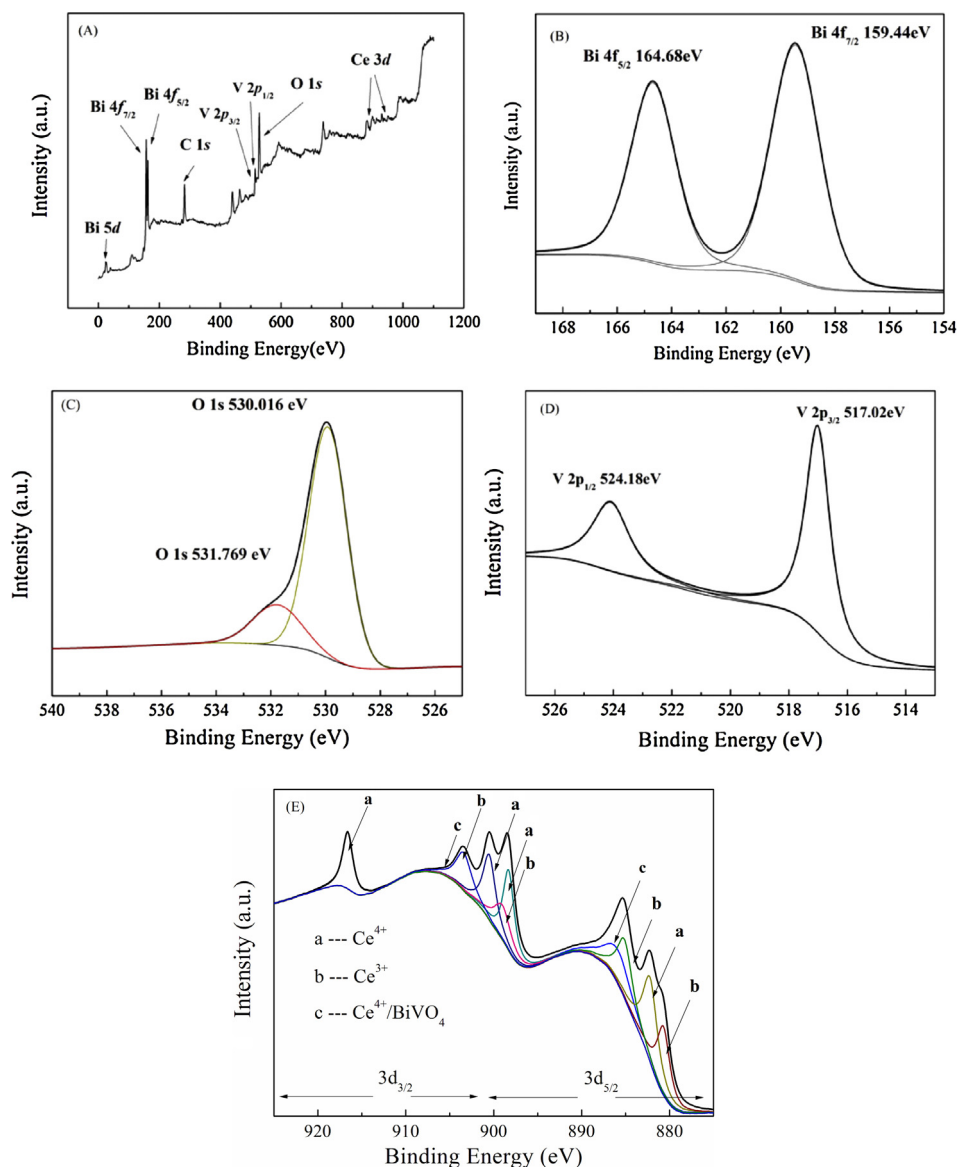
Fig. 4. XPS analysis of 5.7 wt.% CeO$_x$/BiVO$_4$ composite photocatalyst: (A) overall XPS spectra of the CeO$_x$/BiVO$_4$ composite photocatalyst; (B) Bi 4f; (C) O 1s; (D) V 2p; and (E) Ce 3d.

chemical environments although several kinds of crystal lattice oxygen atoms were found in the CeO$_x$/BiVO$_4$ composites [13]. After the sub-peak processing, the weak peak for O 1s was located at about 531.77 eV because of the formation of O—H bonds [24], Fig. 4(D) presents the doublet peaks located at 517.02 and 524.18 eV, which corresponded to V 2$p_{3/2}$ and V 2$p_{1/2}$, respectively. For the monoclinic BiVO$_4$, these two characteristic peaks were related to V^{5+} cations in the crystal lattice. Moreover, no other signal of V^{5+} species was found, which demonstrated that VO$_4^{3-}$ was the only form of V^{5+}.

Fig. 4(E) shows that the Ce 3d spectra were composed of two multiplets (i.e., 3$d_{3/2}$ and 3$d_{5/2}$) with ten peaks after the sub-peak processing. The peaks b located at about 880.71 and 885.29 eV in the low binding energy region and at about 899.29 and 903.48 eV in the high binding energy region were respectively assigned to Ce 3$d_{5/2}$ and Ce 3$d_{3/2}$. These states corresponded to the final states of 3$d^9 4f^1$ and 3$d^9 4f^2$ [25] considering the spin–orbit splitting, which indicated the presence of Ce^{3+} in cerium oxide. Peaks a and c at 882.54, 887.06, and 898.47 eV and their spin–orbit splitting peaks at 900.62, 905.98, and 916.65 eV were attributed to Ce 3$d_{5/2}$ and Ce 3$d_{3/2}$ of Ce^{4+} as a result of the 3$d^9 4f^1$, 3$d^9 4f^2$, and 3$d^9 4f^0$ final

states [26]. These results demonstrated the mixed valence state of the cerium species (+3 and +4). Meanwhile, the peak intensity and area revealed that CeO$_2$ was the dominant component in the cerium oxide. Peaks c assigned to Ce 3$d_{5/2}$ and Ce 3$d_{3/2}$ located at about 887.06 and 905.98 eV took red shifts of ca. 1.5 eV in comparison with the result reported earlier [27,28]. This finding may be caused by the interaction between Ce^{4+} and BiVO$_4$ in the heterojunction nanostructure on the CeO$_x$/BiVO$_4$ composite surface, which diminished the O–Ce binding energy in the CeO$_2$ crystal lattice to some degree.

3.4. Optical properties

The optical properties of the pure BiVO$_4$, CeO$_x$ and CeO$_x$/BiVO$_4$ composites were investigated using the UV–vis diffuse reflectance spectroscopy (Fig. 5). The absorption intensities of the CeO$_x$/BiVO$_4$ composites in the visible-light range were obviously higher than those of both the pure BiVO$_4$ and CeO$_x$.

The absorption edges of the CeO$_x$/BiVO$_4$ composites showed a little shift toward the visible region upon loading the cerium oxide nanodots onto the BiVO$_4$ surface. This result may imply that no
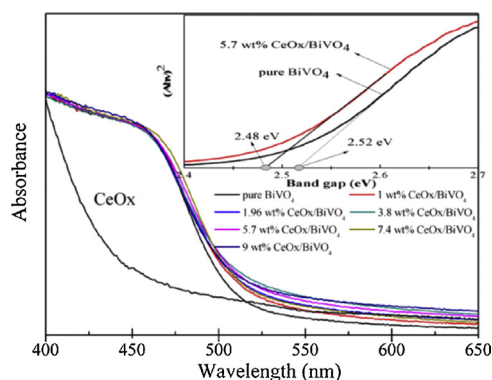
Fig. 5. DRS spectra of the pure $BiVO_4$, CeO_x and $CeO_x/BiVO_4$ series of composite photocatalysts; the inset shows the band gap energy of the pure $BiVO_4$ and 5.7 wt.% $CeO_x/BiVO_4$ composite.

Fig. 7. Kinetics of the MB decomposition over different samples.

doping level was found between the conduct and valence bands of $BiVO_4$ because Ce was only loaded on the $BiVO_4$ surface to form a heterojunction without being anchored into the crystal lattice. The optical band gap for the semiconductor photocatalysts was estimated using the following equation:

$$(Ah\nu) = a(h\nu - E_g)^{n/2}$$

where A is the absorption coefficient near the absorption edge; h is the Planck's constant with the unit of eV; a is a constant; E_g is the absorption band gap energy; and n represented 1 and 4 for the direct and indirect band gap semiconductors, respectively [29,30]. $BiVO_4$ have a direct band gap, and n was 1 herein. The inset of Fig. 5 shows the curve of $(Ah\nu)^2$ versus $h\nu$ of pure $BiVO_4$ and 5.7 wt.% $CeO_x/BiVO_4$ composite. The band gaps of 5.7 wt.% $CeO_x/BiVO_4$ and pure $BiVO_4$ were estimated to be about 2.48 and 2.52 eV, respectively. Fig. 5 shows that the CeO_x presented weakly absorption for visible-light and the band gap of CeO_x was calculated to be about 2.76 eV, and all the $CeO_x/BiVO_4$ composite series possessed a similar band gap of ∼2.48 eV, which was lower than that for both pure $BiVO_4$ and CeO_x. This result implied that the $CeO_x/BiVO_4$ composites could generate more electron–hole pairs than pure $BiVO_4$ under visible-light irradiation, which resulted in a higher photocatalytic performance.

3.5. Effect of Ce on the photocatalytic properties

The photocatalytic performance of the prepared pure $BiVO_4$, CeO_x and $CeO_x/BiVO_4$ composites with a heterojunction nanostructure was evaluated by examining the photodegradation of MB under visible-light irradiation (Fig. 6).
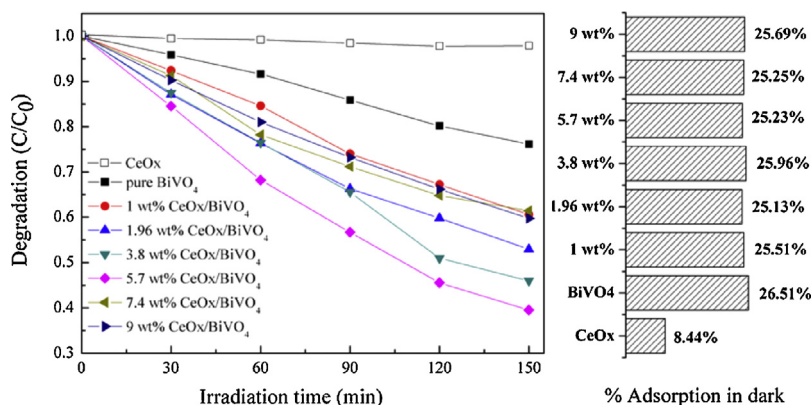
Generally, the different concentration of MB adsorbed on the photocatalyst surface will give a great influence on the photocatalytic activity, so the adsorption ratio was recorded when adsorption–desorption equilibrium was achieved before irradiation. Fig. 6 shows that all the samples except CeO_x presented the similar capacity for MB adsorption, though having different surface area. And CeO_x could hardly degrade MB under visible-light irradiation. The photodegradation rate of MB for the pure $BiVO_4$ was 24% after 150 min of irradiation, which indicated that only a little part of MB was degraded (Fig. 6). All the $CeO_x/BiVO_4$ composites clearly showed a better photocatalytic performance than both the pure $BiVO_4$ and CeO_x. This observation implied that CeO_x deposited on the $BiVO_4$ surface and the heterojunction nanostructure played an important role in improving the photocatalytic activity. Fig. 6 also demonstrates that the photodegradation rate of MB using the $CeO_x/BiVO_4$ composites initially increased along with the increase of the cerium content in the order of 1 wt.% $CeO_x/BiVO_4$ (38%), 1.96 wt.% $CeO_x/BiVO_4$ (47%), 3.8 wt.% $CeO_x/BiVO_4$ (55%), and 5.7 wt.% $CeO_x/BiVO_4$ (61%). The photodegradation ratio of MB decreased to 37% and 41%, respectively, when the mass ratio of CeO_x was up to 7.4 and 9 wt.%. A pseudo-first-order kinetic model was used to fit the degradation data using $\ln(C_0/C) = kt + a$, where k is the apparent reaction rate constant (Fig. 7). The kinetic parameters for each photocatalyst were calculated and listed in inset of Fig. 7. The figure reveals that 5.7 wt.% $CeO_x/BiVO_4$ had the best photodegradation performance. Accordingly, 5.7 wt.% $CeO_x/BiVO_4$ showed a much higher photocatalytic activity than pure $BiVO_4$. Moreover, further increasing the cerium content on the $BiVO_4$ surface will lead to decrease of the photocatalytic performance under visible-light. Three plausible reasons were thought to result in this

Fig. 6. Comparison of the adsorption and degradation ratio of MB using the pure $BiVO_4$, CeO_x and $CeO_x/BiVO_4$ series of composites in dark and under visible-light irradiation.
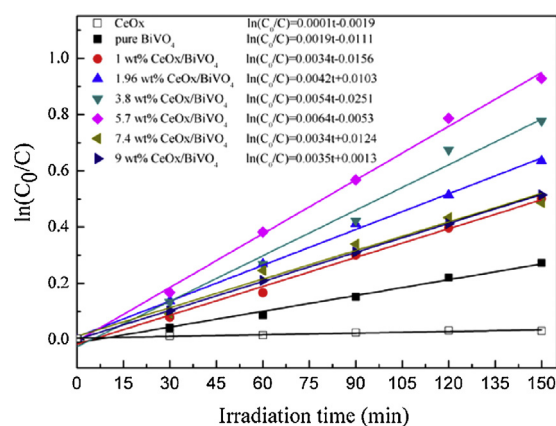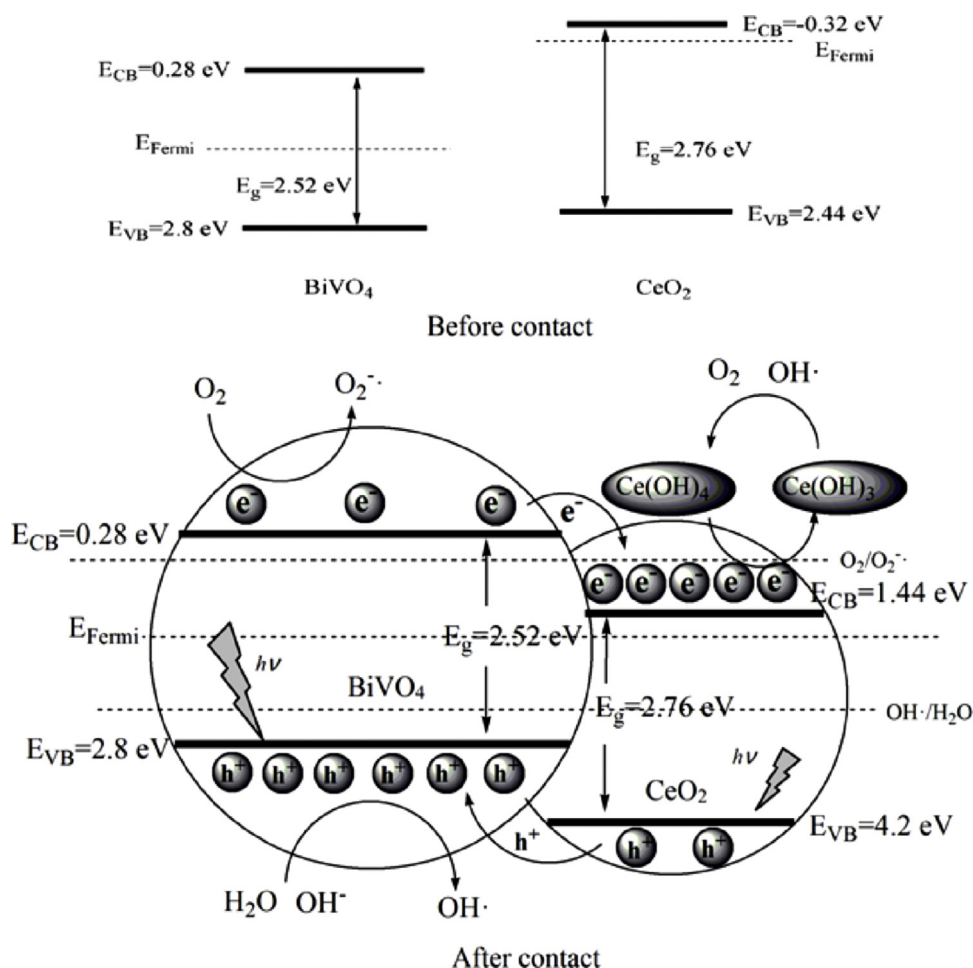
Fig. 8. Energy band diagram for the CeO$_x$/BiVO$_4$ heterojunction nanostructure photocatalyst after the thermodynamic equilibrium.

finding: (i) excess CeO$_x$ may cover the active sites on the BiVO$_4$ surface and thereby reduce the charge-separation efficiency [31,32]; (ii) excess CeO$_x$ may be the recombination center of the photogenerated electron–holes because of the short-circuiting mechanism [33]; and (iii) the size of the composite photocatalysts obviously increased when the cerium content was up to 9 wt.% (Fig. 2(D), Table 1), which then may reduce the transmission efficiency of photogenerated electron–holes to the composite surface.

A possible mechanism for the MB photodegradation over the CeO$_x$/BiVO$_4$ heterojunction nanostructure under visible-light irradiation can be proposed based on the preceding data to illustrate the reasons of the high photocatalytic activity of the CeO$_x$/BiVO$_4$ composites compared to the pure BiVO$_4$. Accordingly, CeO$_x$ will be treated as CeO$_2$ in this section. The band edge positions of the conduction band (CB) and the valence band (VB) of a semiconductor were calculated as follows [12]:

$$E_{CB} = \chi - E^e - \frac{1}{2}E_g \tag{1}$$

$$\chi = \frac{1}{2}(A_f + I_1) \tag{2}$$

$$E_g = E_{VB} - E_{CB} \tag{3}$$

where χ is the absolute electronegativity of a semiconductor (i.e., 5.56 and 6.04 eV for CeO$_2$ and BiVO$_4$ [10,34], respectively); A_f and I_1 are the atomic electron affinity and the first ionization potential, respectively; E^e is the energy of free electrons on the hydrogen scale (i.e., about 4.5 eV); and E_g is the band gap energy of the semiconductor. The calculation result showed that the bottom of the

conduction band of BiVO$_4$ was 0.28 eV, whereas the top of the valence band was 2.8 eV. The energy of the conduction and valence bands of CeO$_2$ were −0.32 and 2.44 eV, respectively. Fig. 8 illustrates the photogenerated electron–hole transfer behavior in the heterojunction nanostructure.

BiVO$_4$ was considered as an intrinsic semiconductor. Hence, the Fermi level in BiVO$_4$ laid in the middle of the conduction band and the valence band [15] which located at around 1.54 eV. The Fermi level of n-type semiconductor generally laid below the bottom of the conduction band by ca. 0.1–0.2 eV [35]. Accordingly, the Fermi level in CeO$_2$ located at around −0.22 eV. The heterojunction nanostructure was formed after the CeO$_x$ tightly deposited on the BiVO$_4$ surface. According to the Fermi level definition, the composites had a uniform Fermi level when the system was in equilibrium. The Fermi level in the composites moved to be around 1.54 eV, which was approximately equal to that of BiVO$_4$ for the low cerium content. Consequently, E_{CB} of CeO$_2$ decreased from −0.32 to 1.44 eV, and E_{VB} decreased from 2.44 to 4.2 eV (Fig. 8). Excited electrons (e^-) were generated from the valence band into the conduction band of BiVO$_4$ when the composites were irradiated under visible-light. Furthermore, the corresponding holes (h^+) were leaving in the valence band. The same process occurred in CeO$_2$, but the quantity of the photogenerated electron–holes was less than that in BiVO$_4$ for the wide band gap. E_{CB} of BiVO$_4$ and CeO$_2$ in the heterojunction nanostructure formed an electric potential of ca. 1.16 eV, which drove the excited electrons (e^-) from the conduction band of BiVO$_4$ into the conduction band of CeO$_2$. Similarly, the holes (h^+) were transferred to the valence band of BiVO$_4$. This process can effectively prevent the photogenerated electrons from
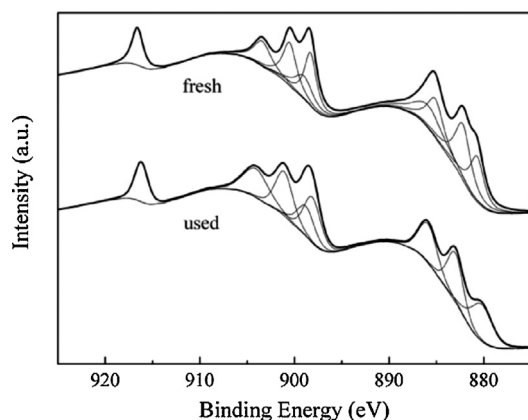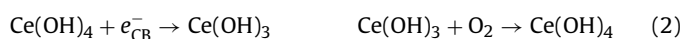
Fig. 9. XPS of cerium in 5.7 wt.% $CeO_x/BiVO_4$ before and after photocatalytic reaction.

Fig. 10. EPR signals of the DMPO-trapped OH• in $BiVO_4$ suspension, CeO_x suspension and 5.7 wt.% $CeO_x/BiVO_4$ suspension without irradiation and without irradiation ($\lambda > 420$ nm).

Fig. 11. PL spectra of the pure $BiVO_4$ and $CeO_x/BiVO_4$ series of composites.

quickly recombining with the holes. According to $E_{(OH•/H2O)}$ in Fig. 8, the holes (h^+) can oxidize the absorbed H_2O and OH^- to hydroxyl radicals (OH•) with a strong oxidizing nature. These holes play an important role in the photocatalytic oxidation process. H_2O_2 was also produced as a consequence of the combination of two hydroxyl radicals (OH•), which can further oxidize OH^- into $O_2H•$ and ensure the constant stream of surface OH• radicals in the photocatalytic process. Furthermore, the photogenerated holes (h^+) in the valence band of $BiVO_4$ can also directly oxidize part of MB. However, only a little of O_2 adsorbed on the surface can be reduced to $O_2^-•$ by electrons (e^-) because most of the electrons (e^-) would stream to the conduct band of CeO_2 with an energy level lower than $E_{(O2/O2-•)}$. Meanwhile, the conduction electrons (e^-) can be captured by surface Ce^{4+}, which was reduced to Ce^{3+}. Ce^{3+} can then be re-oxidized to Ce^{4+} by O_2 or OH• to form a cycle reaction. This cycle reaction made an important contribution to the separation of photogenerated electron–hole pairs. Fig. 9 shows the chemical state of the cerium which was after photocatalytic reaction.

According to the XPS analysis above (Fig. 4(E)), the cerium species maintained the mixed chemical state after the photoreaction though having some difference, which implies that the cycle reaction of cerium maybe do exist. The continuous electron capture function of cerium appeared to be another important function of cerium oxides in the heterojunction nanostructure to improve the photocatalytic performance of $BiVO_4$. The main reactions were concluded as follows:

$$BiVO_4 + h\nu \rightarrow e_{CB}^- + h_{VB}^* \qquad CeO_2 + h\nu \rightarrow e_{CB}^- + h_{VB}^* \qquad (1)$$

$$Ce(OH)_4 + e_{CB}^- \rightarrow Ce(OH)_3 \qquad Ce(OH)_3 + O_2 \rightarrow Ce(OH)_4 \qquad (2)$$

$$H_2O + h_{VB}^+ \rightarrow OH^• + H^+ \qquad (3)$$

$$OH^• + OH^• \rightarrow H_2O_2 \qquad (4)$$

$$H_2O_2 + OH^- \rightarrow O_2H^• + H_2O \qquad (5)$$

In order to clarify the charge transfer between $BiVO_4$ and CeO_x in heterojunction, we detected the involved active species forming in the photocatalytic reaction under visible-light irradiation. Spin-trapping electron paramagnetic resonance (EPR) technique was employed to detect the existence of the hydroxyl radicals (OH•) in the $CeO_x/BiVO_4$ system using DMPO as trapping agent. The results are shown in Fig. 10. There was no signal when all the suspensions were in dark. However, four characteristic peaks with intensity 1:2:2:1 for DMPO-trapped OH• were observed in $CeO_x/BiVO_4$ suspension under visible-light irradiation, indicating that the hydroxyl radicals (OH•) was formed. By contrast, the peaks intensity in $BiVO_4$ suspension was so weak and there was even no signal in CeO_x suspension under visible-light irradiation. It implies that more active
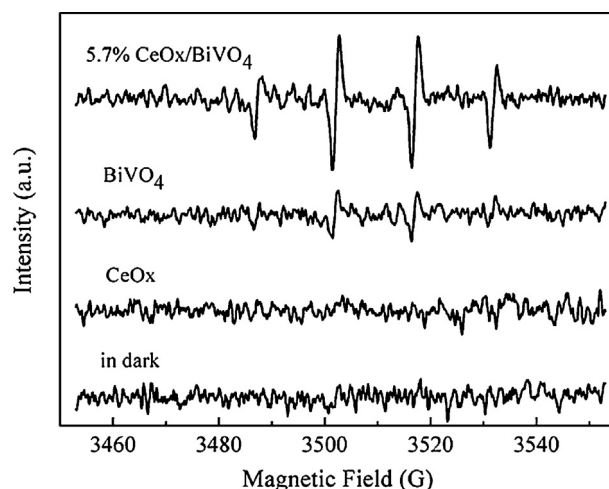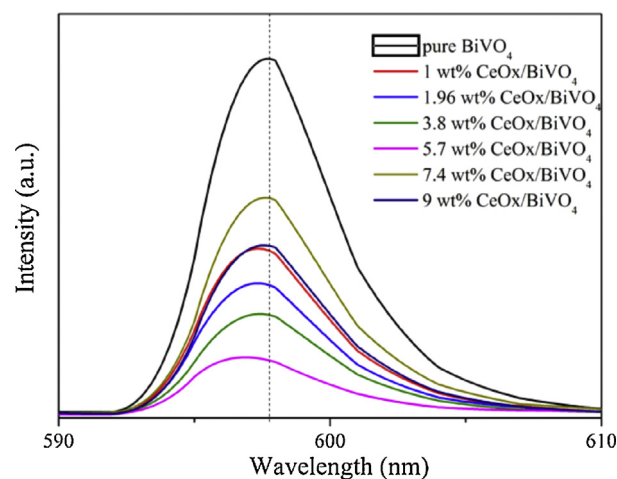
species were produced after the formation of heterojunction structure.

The PL test of the photocatalysts was used to illustrate the fact that the photogenerated electron–hole pairs were effectively separated. The pure $BiVO_4$ and $CeO_x/BiVO_4$ composites were excited at 300 nm wavelength. Fig. 11 presents the PL spectra.

The peak with the largest intensity attributed to the pure $BiVO_4$ appeared at around 600 nm, which was also actually a character PL peak of the monoclinic $BiVO_4$ [8,19]. The luminescence corresponded to the recombination of the hole formed in the O 2p band and the electron in the V 3d band. The intensity of the PL peaks decreased after the heterojunction nanostructure formation in the $CeO_x/BiVO_4$ series of composites (Fig. 11). With the Ce mass ratio increasing from 1 wt.% to 5.7 wt.% in the heterojunction, the PL peak intensity declined and the lowest peak intensity was observed for the 5.7 wt.% $CeO_x/BiVO_4$ composite. It implied that the recombination of the photogenerated electrons–holes was greatly suppressed. The peak intensity raised again when the cerium content further increased. This intensity remained highly consistent with the photocatalytic performance of the samples (Figs. 6 and 7). Most importantly, the blue shift of peaks to the lower wavelength after cerium was introduced was clearly observed (Fig. 11). This shift was related to the change of the Ce ion valence from 4^+ to 3^+ corresponding to the transition of the electrons from the 4f band

to the valence band of CeO$_2$ [36,37]. To the best of our knowledge, this is the first study to show that the process of photogenerated electrons trapped by valence-variable ions in the semiconductor was indirectly proved by the change in the photoluminescence spectrum, albeit having been recently proposed [33,38]. The higher number of shifts to a lower wavelength implied the better effect of cerium species on separating electron–holes, which corresponded to a better photocatalytic performance.

4. Conclusion

In summary, CeO$_x$/BiVO$_4$ composite photocatalysts with heterojunction structure were synthesized by hydrothermal and ion impregnation method. The structural studies revealed that all the photocatalysts prepared exhibited the typical pattern of monoclinic BiVO$_4$ and the cerium oxides were in 5 nm nanodots which deposited tightly on the surface of BiVO$_4$. The component of the composites, especially for cerium, was confirmed by XPS analysis. The optimum mole ratio of the CeO$_x$/BiVO$_4$ composites was found to be 5.7 wt.%, which showed the best photocatalytic performance in degradation of MB under visible-light irradiation. The possible mechanism was discussed based on heterojunction structure, and the charge transfer between BiVO$_4$ and CeO$_x$ in heterojunction was demonstrated by detecting the involved active species using EPR spectra. Another important role of cerium in separation of electron–hole pairs through trapping excited electrons was proved using PL indirectly. Further detailed studies to fully understand the mechanism about improving the photocatalytic performance of BiVO$_4$ under visible-light are ongoing in our laboratory.

Acknowledgment

References

[1] H. Fan, T. Jiang, H. Li, D. Wang, L. Wang, J. Zhai, D. He, P. Wang, T. Xie, J. Phys. Chem. C 116 (2012) 2425–2430.
[2] Y. Zhang, G. Li, X. Yang, H. Yang, Z. Lu, R. Chen, J. Alloys Compd. 551 (2013) 544–550.
[3] P. Wang, B. Huang, X. Qin, X. Zhang, Y. Dai, J. Wei, M. Whangbo, Angew. Chem. Int. Ed. 47 (2008) 7931–7933.
[4] D. Yang, H. Liu, Z. Zheng, Y. Yuan, J. Zhao, E. Waclawik, X. Ke, H. Zhu, J. Am. Chem. Soc. 131 (2009) 17885–17893.
[5] X. Wei, T. Xie, D. Xu, Q. Zhao, S. Pang, D. Wang, Nanotechnology 19 (2008) 275707–275712.
[6] H.G. Kim, P.H. Borse, W.Y. Choi, J.S. Lee, Angew. Chem. Int. Ed. 44 (2005) 4585–4589.
[7] H. Tada, T. Mitsui, T. Kiyonaga, T. Akita, K. Tanaka, Nat. Mater. 5 (2006) 782–786.
[8] C. Yu, K. Yang, J. Yu, F. Cao, X. Li, X. Zhou, J. Alloys Compd. 509 (2011) 4547–4552.
[9] H. Xu, H. Li, C. Wu, J. Chu, Y. Yan, H. Shu, Z. Gu, J. Hazard. Mater. 153 (2008) 877–884.
[10] H. Jiang, H. Endo, H. Natori, M. Nagai, K. Kobayashi, Mater. Res. Bull. 44 (2009) 700–706.
[11] P. Chatchai, Y. Murakami, S. Kishioka, A.Y. Nosaka, Y. Nosaka, Electrochim. Acta 54 (2009) 1147–1152.
[12] H. Xu, H. Li, C. Wu, J. Chu, Y. Yan, H. Shu, Mater. Sci. Eng. B 147 (2008) 52–56.
[13] J. Su, X. Zou, G. Li, X. Wei, C. Yan, Y. Wang, J. Zhao, L. Zhou, J. Chen, J. Phys. Chem. C 115 (2011) 8064–8071.
[14] H. Jiang, M. Nagai, K. Kobayashi, J. Alloys Compd. 479 (2009) 821–827.
[15] Y. Hu, D. Li, Y. Zheng, W. Chen, Y. He, Y. Shao, X. Fu, G. Xiao, Appl. Catal. B: Environ. 104 (2011) 30–36.
[16] L. Guo, D. Wang, F. Fu, X. Qiang, F. Zhang, Appl. Chem. Ind. 41 (2012) 260–262.
[17] J. Sun, X. Li, Q. Zhao, J. Ke, D. Zhang, J. Phys. Chem. C 118 (2014) 10113–10121.
[18] Z.M. El-Bahy, A.A. Ismail, R.M. Mohamed, J. Hazard. Mater. 166 (2009) 138–143.
[19] Y. Xie, C. Yuan, X. Li, Mater. Sci. Eng. B 117 (2005) 325–333.
[20] A. Kudo, K. Omori, H. Kato, J. Am. Chem. Soc. 121 (1999) 11459–11467.
[21] G. Li, D. Zhang, J. Yu, Chem. Mater. 20 (2008) 3983–3992.
[22] D. Zhang, H. Fu, L. Shi, J. Fang, Q. Li, J. Solid State Chem. 180 (2007) 654–660.
[23] H. Wang, Z. Wu, Y. Liu, J. Phys. Chem. C 113 (2009) 13317–13324.
[24] M. Futsuharaa, K. Yoshioka, O. Takai, Thin Solid Films 317 (1998) 322–325.
[25] C. Korsvik, S. Patil, S. Seal, W.T. Self, Chem. Commun. 8 (2007) 1056–1058.
[26] E. Beche, P. Charvin, D. Perarnau, S. Abanades, G. Flamant, Surf. Interface Anal. 40 (2008) 264–267.
[27] L. Qiu, F. Liu, L. Zhao, Y. Ma, J. Yao, Appl. Surf. Sci. 252 (2006) 4931–4935.
[28] Y. Tong, Z. Li, X. Lu, L. Yang, W. Sun, G. Nie, Z. Wang, C. Wang, Electrochim. Acta 95 (2013) 12–17.
[29] H. Fu, L. Zhang, W. Yao, Y. Zhu, Appl. Catal. B: Environ. 66 (2006) 100–110.
[30] H. Jiang, H. Dai, J. Deng, Y. Liu, L. Zhang, K. Ji, Solid State Sci. 17 (2013) 21–27.
[31] L. Ge, Mater. Lett. 62 (2008) 926–928.
[32] X. Zhang, Y. Zhang, X. Quan, S. Chen, J. Hazard. Mater. 167 (2009) 911–914.
[33] A. Zhang, J. Zhang, J. Hazard. Mater. 173 (2010) 265–272.
[34] G. Magesh, B. Viswanathan, R.P. Viswanath, T.K. Varadarajan, Indian J. Chem. 48 (2009) 480–488.
[35] S.R. Morrison, Electrochemistry at Semiconductor and Oxidized Metal Electrodes, Plenum Press, New York, 1980.
[36] F. Gao, G. Li, J. Zhang, F. Qin, Z. Yao, Z. Liu, Z. Wang, L. Lin, Chin. Phys. Lett. 18 (2001) 443–448.
[37] S. Yu, H. Colfen, A. Fischer, Colloids Surf. A 243 (2004) 49–52.
[38] A.S. Weber, A.M. Grady, R.T. Koodali, Catal. Sci. Technol. 2 (2012) 683–693.